JPL PUBLICATION 78-91

Application of Digital Image Processing Techniques to Astronomical Imagery 1978

Jean J. Lorre

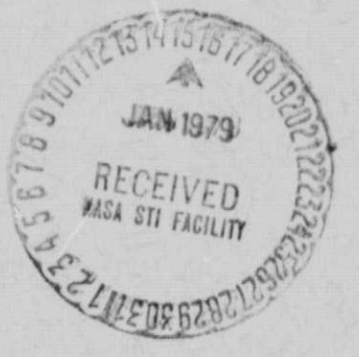

November 1, 1978

National Aeronautics and
Space Administration

Jet Propulsion Laboratory
California Institute of Technology
Pasadena, California

JPL PUBLICATION 78-91

Application of Digital Image Processing Techniques to Astronomical Imagery 1978

Jean J. Lorre

November 1, 1978

National Aeronautics and
Space Administration

Jet Propulsion Laboratory
California Institute of Technology
Pasadena, California

The research described in this publication was carried out by the Jet Propulsion Laboratory, California Institute of Technology, under NASA Contract No. NAS7-100.

PREFACE

The work described in this report was performed by the Earth and Space Sciences Division of the Jet Propulsion Laboratory.

ACKNOWLEDGMENTS

The activities described in this report were encouraged and supported by Dr. Charles O'Dell, Space Telescope Project Scientist at Marshall Space Flight Center, Dr. Nancy Roman and Dr. Jeffrey Rosendahl at NASA Headquarters. William B. Green, Manager of the Science Data Analysis Section that includes the JPL Image Processing Laboratory, was responsible for initiating the project. I wish to thank Dr. John Beverley Oke and Ms. Barbara Zimmermann for the silicon vidicon spectra, Dr. Alan Dressler for plates of Abell 655, Dr. Thomas Kuiper for the radio data of Lick Hα101 and his helpful suggestions, and Dr. Ivan King for plates of NGC6218.

ABSTRACT

Several areas of application of image processing to astronomy have been identified and developed in this report. These areas include (1) geometric and radiometric decalibration of vidicon-acquired spectra, (2) automatic identification and segregation of stars from galaxies, and (3) display of multiband radio maps in compact and meaningful formats. Examples are presented of these techniques applied to a variety of objects. The techniques were developed at the Image Processing Laboratory of the Jet Propulsion Laboratory.

CONTENTS

Figures

SECTION I

INTRODUCTION

Astronomy has traditionally made great use of imagery, but this data has almost exclusively been evaluated via the photographic process. With the advent of the unmanned planetary missions and digital cameras, techiques for processing digital images have been developed and are beginning to be applied in astronomy. The advantages of digital images over photographic ones is very great and, with the development of new algorithms and cameras, becomes greater all the time. It is thus of importance to search for applications and disseminate digital techniques to the astronomical community at large. When Space Telescope becomes operational, the quantity and unprecedented quality of the calibrated digital images returned will call for every available processing means at our disposal. This report is intended to provide a few of those means.

This work was performed during 1978 at the Image Processing Laboratory (IPL) of JPL under FY78 RTOP #389-41-01. It represents a continuing effort (Ref. 1) to identify and develop new image processing applications to astronomy. Additional goals of this research are the further education of the astronomical community in digital image processing techniques and the expansion of methods for analysis of high-quality space telescope imagery when it becomes available. Hopefully others will be inspired to find applications to their own disciplines.

This report is divided into six sections. Sections II through IV present techniques applied to a major topic. The data used and the techniques involved are described in detail along with photographs and plots of the results. Section V states conclusions which can be made as a result of this work. This report illustrates image processing and does not interpret the physical significance of results which accrue from the data. The role of data interpretation resides with the collaborating astronomer. Image processing is a vehicle to strengthen and simplify his task.

SECTION II

DECALIBRATION OF VIDICON SPECTRA

A silicon vidicon camera can produce high-quality digital spectra if the geometric and radiometric distortions can be calibrated and subsequently removed. The geometric distortion is due to deflection of the readout beam, and the radiometric distortion is caused by spatial sensitivity variations across the semiconductors, the latter being a function of wavelength as well. The response of each point is, however, linear but with unknown slope and offset. Figure 1 presents a mosaic of many spectra. These distorted spectra represent the data as they are produced by the vidicon. Each spectrum has been contrast-enhanced separately in order to render them all visible simultaneously. File 1 is a comparison spectrum, file 2 contains the spectrum of an incandescent source, file 3 is a dark current picture, and most of the other files represent stellar spectra with some degree of night sky superimposed as a broad background. It is possible, given the images in files 1-3, to generate decalibration files which will eliminate most of the vidicon-induced artifact. Eventually a picture will be produced which contains an undistorted spectrum where each pixel (picture element) has a known wavelength and an intensity value in the same linear system as all the other pixels.

Figure 2 represents various stages in the decalibration process. The top four spectra of Fig. 2, from the top down, are the original distorted comparison, incandescent, dark current, and the subject spectrum to be decalibrated.

Digital spectra were provided by Dr. John Beverly Oke of Caltech and Barbara Zimmermann of Caltech. The spectra were obtained on a silicon vidicon as halfword values in 64 lines of 512 samples per line. The calibration and decalibration steps required to correct the vidicon spectra are listed below in the order that they are performed:

(1) Trace the subject spectrum to be decalibrated across the image, recording the centroids (less background) of the spectrum for each column in the picture.

(2) Fit a third-order polynomial to the centroid positions. The characteristic "s" shaped vertical distortion is well-modeled with this order function.

(3) Trace each of the comparison lines in the comparison line spectrum, computing centroids for each row.

(4) Fit a straight line to each comparison line.
In the fifth row down in Fig. 2, the closest integer pixels to each centroid located have been set to white, revealing the history of the centroid tracking algorithm for both the stellar and comparison spectrum superimposed.

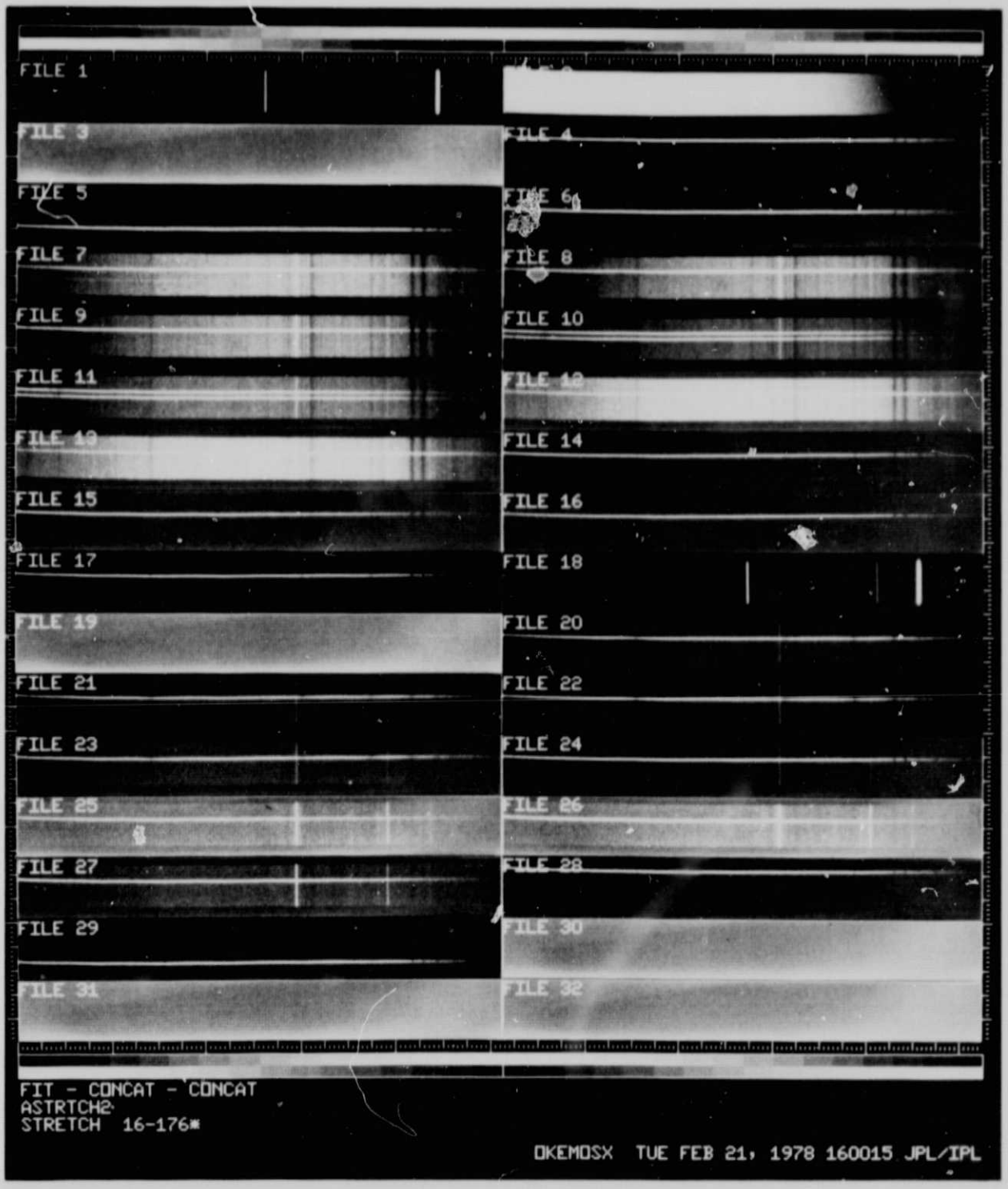

Figure 1. A mosaic of undecalibrated spectra as produced by the silicon vidicon. Each spectrum has been contrast-enhanced separately. File 1 contains a comparison spectrum. File 2 contains the spectrum of an incandescent lamp. File 3 contains a dark current image. Most of the other files contain stellar spectra with the night sky lines superimposed

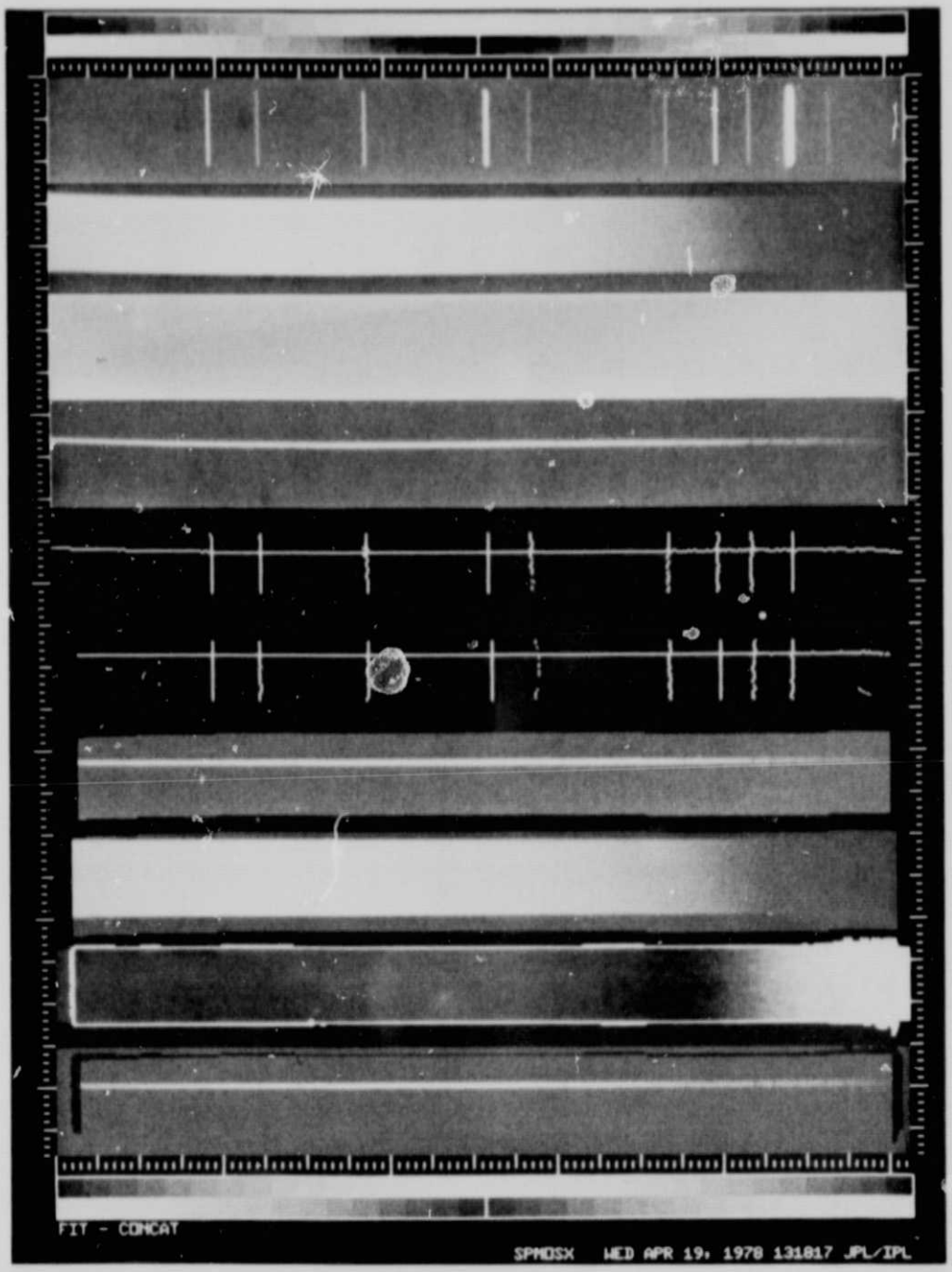

Figure 2. A mosaic of ten spectra depicting various stages in the decalibration process. From the top down each spectrum represents: (1) distorted comparison spectrum, (2) distorted incandescent spectrum, (3) distorted dark current, (4) distorted subject spectrum, (5) superimposed trace of points along the subject spectrum and comparison lines, (6) the trace after geometric correction, (7) geometrically corrected subject spectrum, (8) geometrically corrected incandescent spectrum, (9) radiometric decalibration file, (10) geometrically and radiometrically corrected subject spectrum

(5) Compute the intersection points where the third-order "s" function crosses each of the linear fits to the comparison lines.

(6) Fit the horizontal intersection points to a fifth-order polynomial, using the known wavelengths of the comparison lines.

(7) Geometrically rectify the subject spectrum using the fifth-order coefficients horizontally and the third-order coefficients vertically (cross-coupling is ignored).

This terminates the geometric phase of the decalibration. Row 6 of Fig. 2 illustrates the history of the centroid tracker on the geometrically corrected subject and comparison spectra, the former of which is now much straighter.

In order to minimize degradation due to pixel intensity interpolation, the Sampling Theorem is used. Because vidicons band-limit the signal to an acceptable degree, the Sampling Theorem is obeyed and there is an optimal interpolation formula. For any fractional (x,y) position in the distorted image, the intensity value there is obtained from (1):

$$I_{x,y} = \sum_{i=x-\delta}^{x+\delta} \sum_{j=y-\delta}^{y+\delta} I_{i,j} \frac{\sin(x-i)\pi}{(x-i)\pi} \frac{\sin(y-j)\pi}{(y-j)\pi} \qquad (1)$$

where i and j are rounded integers and δ is the half width of the filter.

(8) Using the same coefficients, geometrically rectify the incandescent and dark current spectra so that they correspond spatially with the subject spectrum. Rows 7 and 8 of Fig. 2 illustrate the subject and incandescent spectra after geometric correction.

(9) Subtract the dark current image from the rectified subject and incandescent spectra.

(10) Average the incandescent spectrum along a vertical column to produce a vector of the one-dimensional profile.

(11) Fit a third-order polynomial to the logarithm of this profile. The polynomial represents a smooth function which should closely resemble the log of a black body distribution. This function will be used to estimate the relative spectral radiance of the incandescent source since the true distribution is unknown.

(12) Generate a radiometric decalibration file picture by dividing at each point the incandescent spectrum into the exponent of the fitted spectral radiance polynomial for that equivalent

wavelength. The decalibration picture is shown as row 9 of Fig. 2.

(13) Decalibrate the subject spectrum by multiplying it by the decalibration file. The completed spectrum is presented as the bottom row of Fig. 2.

(14) Produce an intensity profile of the spectrum by integrating the spectrum in columns after subtracting the sky using background points above and below the spectrum.

An example of such an intensity profile is given in Fig. 3. This is the spectrum of a white dwarf processed using the above steps.

The coefficients used to determine the geometric correction and the decalibration file can be reused to decalibrate other spectra to the same coordinate system. Residuals obtained from fitting the calibration lines indicate that the wavelength of any feature can be obtained to about 0.5 A. It is important to realize, however, that geometric distortion in vidicons is dependent upon the structure and intensity of the image and is thus unique to each spectrum. This is due to deflection of the readout beam by the charged semiconducting cathode upon which the image lies. It is thus desirable to geometrically rectify each image on a custom basis. To obtain optimal rectification, fiducial marks should be placed on the cathode platen to provide a reference for correcting the vidicon-induced distortion. Then the wavelength calibration can be performed as a separate invariant transformation.

The digital nature of these spectra provides a cost-effective advantage over the photographic method. Decalibration can be performed on a routine basis without human intervention, irrespective of the nature of the spectrum. Intensity profiles can be produced in the same intensity and geometric reference system, taking advantage of an unchanging detector.

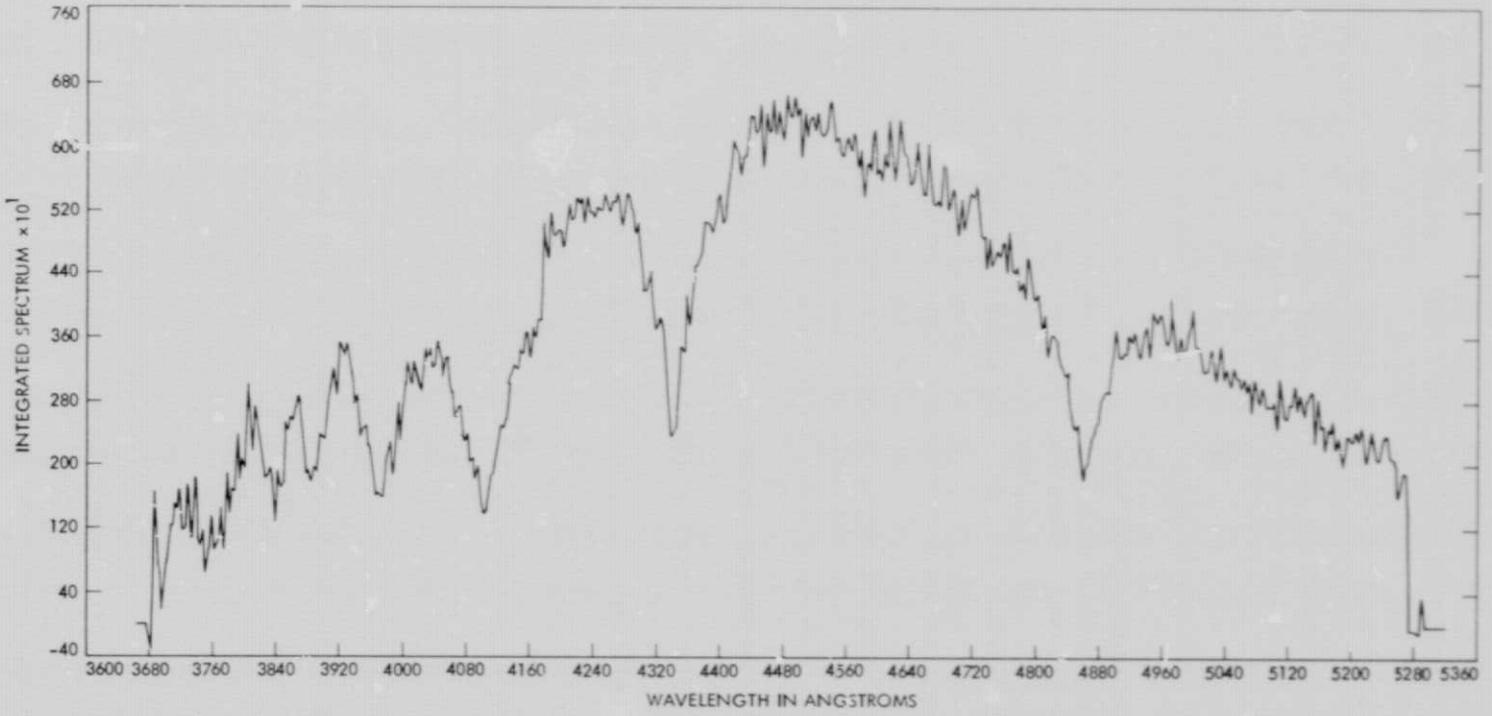

Figure 3. The integrated spectrum of a white dwarf decalibrated using the above process. The wavelength axis is good to 0.5 Å and the spectrum is free of night sky lines

SECTION III

STAR-GALAXY CLASSIFICATION

The purpose of the following section is to illustrate a technique by which a digital image can be analyzed automatically to locate and segregate between stars and galaxies. A constraint was adopted which limited the range of available classification methods. The constraint required that as much usefully interpretable information be collected as possible on each object during the course of the classification. As a consequence it was decided to select a polar coordinate transformation for each candidate object from which such parameters as mean radial profile and the distribution of intensity as a function of azimuth could be generated.

Three parameters were used to segregate between stars and galaxies:

(1) The standard deviation of a gaussian fitted to the mean radial profile.

(2) The amplitude of a gaussian fitted to the mean radial profile.

(3) The eccentricity of the azimuthal intensity distribution.

When a volume is constructed whose axes represent each of the above parameters and the positions of stars and galaxies are plotted in this volume, the two classes fall in separate parts of the space everywhere but at the lowest intensity regime. By segregating the space into star, galaxy, and ambiguous regions, unknown objects can be classified with good assurance of success.

The following section outlines the steps performed by the classifier to determine the nature of each object:

(1) Before any classification can be performed, a catalog of all objects on the plate must be generated (Ref. 1). This catalog contains information on the intensity, area, and centroids of objects. This step extracts features of interest for the cataloger to analyze, using a simple above-intensity threshold criterion.

(2) Select, in turn, each catalog entry and read an area encompassing the object into main storage, converting each pixel value to intensity by a lookup table which characterizes the HD curve of the photographic emulsion.

(3) Optionally search each area in question to determine the number of objects it contains. This step may be necessary (although it was not needed in the case of Abell 655) if the region is highly crowded, as the catalog is not sophisticated enough to separate blended objects. The method used is to grow a region around the largest intensity value contained in that portion of the picture in main storage, using a

minimum rate of descent algorithm. Each pixel within the grown region is flagged with the identifier of the object. The next largest remaining unflagged intensity value is selected and a second region is grown, etc. New objects can be identified provided they do not start adjacent to a previously flagged pixel (in which case they share the adjacent pixel's ID). The region grower operates by:

(a) Selecting the largest of its eight neighboring pixels.

(b) Checking to verify that the neighbor has more than one flagged neighbor.

(c) Moving over to that neighbor's position.

(d) Flagging the pixel with the object ID.

(e) Executing step a again.

If in step b a pixel has only one flagged neighbor, the region grower stops since it is now operating in the background noise.

(4) Fit a least square plane to points lying on the border of a circle which is centered on the object and subtract the plane from the object. This removes the local background from each object. If more than one object is contained within the area read, this and the following steps are performed upon each one of them in order of ascending object brightness.

(5) Generate a polar coordinate image for each object centered at its centroid position. Each line of the polar coordinate image represents a radial profile from the centroid outward, the lines progressing from 0 to 2π. Spline interpolation is used to interpolate intensity values between adjacent pixels. The resolution is such that 1:1 magnification exists at the edge of the circular area.

(6) Compute a vector by integrating the polar coordinate image in the radial direction. This vector represents at each point the sum of intensity radially outward at a particular azimuth.

(7) Compute the position angle of the main axis and the eccentricity by least squares from the above vector.

(8) Optionally reinterpolate the polar coordinate image on a line-by-line basis such that the sums of intensities along each line (radial direction) are the same as the sum of the averages before interpolation. This step removes the eccentricity of galaxies seen non-face on.

(9) Compute the mean radial profile from the sums of the columns of the polar coordinate image. An option at this stage

is to truncate nonmonotonically decreasing pixels from each of the individual profiles (lines).

(10) Fit a gaussian function to the mean radial profile, ignoring those points on the profile below a percentage of the peak intensity.

(11) In the event that more than one object is detected within the area read into main storage, the current object, within the radius used, is replaced by the least squares plane originally subtracted from it and the above steps are repeated for each of the remaining objects.

(12) The pertinent information derived such as amplitude, intensity standard deviation and eccentricity is stored in the catalog.

(13) When each object contained in the catalog has been evaluated a plot is made of the amplitude vs the standard deviation of the fitted gaussian. Each point is identified by the ID number in the catalog. A picture is generated with each object flagged by its ID Number. From this information, the analyst can divide the classification space into three zones for stars, galaxies, and everything else too faint to discriminate (unclassified). Judgment can be made visually by inspecting objects bright enough to obviously fall into certain classes.

(14) When the classification space has been divided up, the program can update the catalog to reflect the status of each object.

The classification program was executed on plates containing only stars and plates containing both stars and galaxies. The stellar-only plates were of the globular cluster NGC6218 and were provided by Dr. Ivan King of the University of California at Berkeley. The other image was a 48" Schmidt plate of the cluster of galaxies Abell 655 and was provided by Dr. Alan Dressler of Hale Observatories. In order to provide a viewable format for the classification space, a two-dimensional format is presented with the gaussian standard deviation as the ordinate and the gaussian amplitude as the abscissa. One must imagine depth as eccentricity although this parameter is only useful for the lower intensity range where the amplitude-standard deviation is not adequate when taken alone.

Figure 4 illustrates two plots of the classification space for the globular cluster NGC6218. The upper plot was made from a plate with an effectively shorter exposure than the one used for the lower plot. In either case, no galaxies are present. Figure 5 illustrates another plot, this time of Abell 655. Figure 5 contains 1200 points, most of which are galaxies. For the case of Abell 655, the space is populated with a horizontal cluster and a vertical cluster, the latter passing both above and below the horizontal cluster and to its left. In the case of NGC6218, the vertical clusterdid not pass above the horizontal cluster (the points which did were mostly blended objects). From this and other diagrams, it is apparent that the cluster represented population groups as follows:

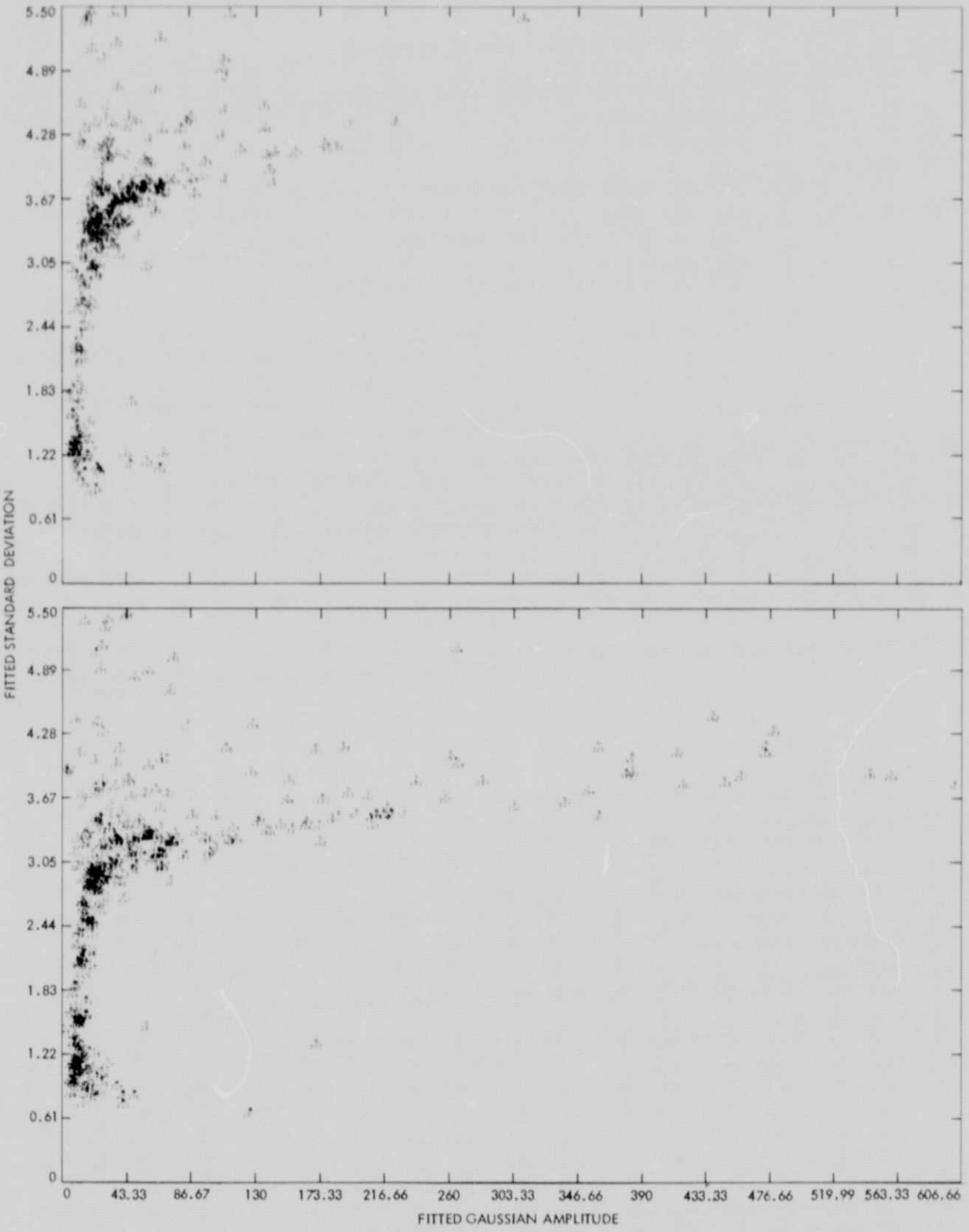

Figure 4. Two plots of the classification space showing the distributions for two plates of NGC6218, a globular cluster. Only stars are present. The lower plot is for the longer effective exposure

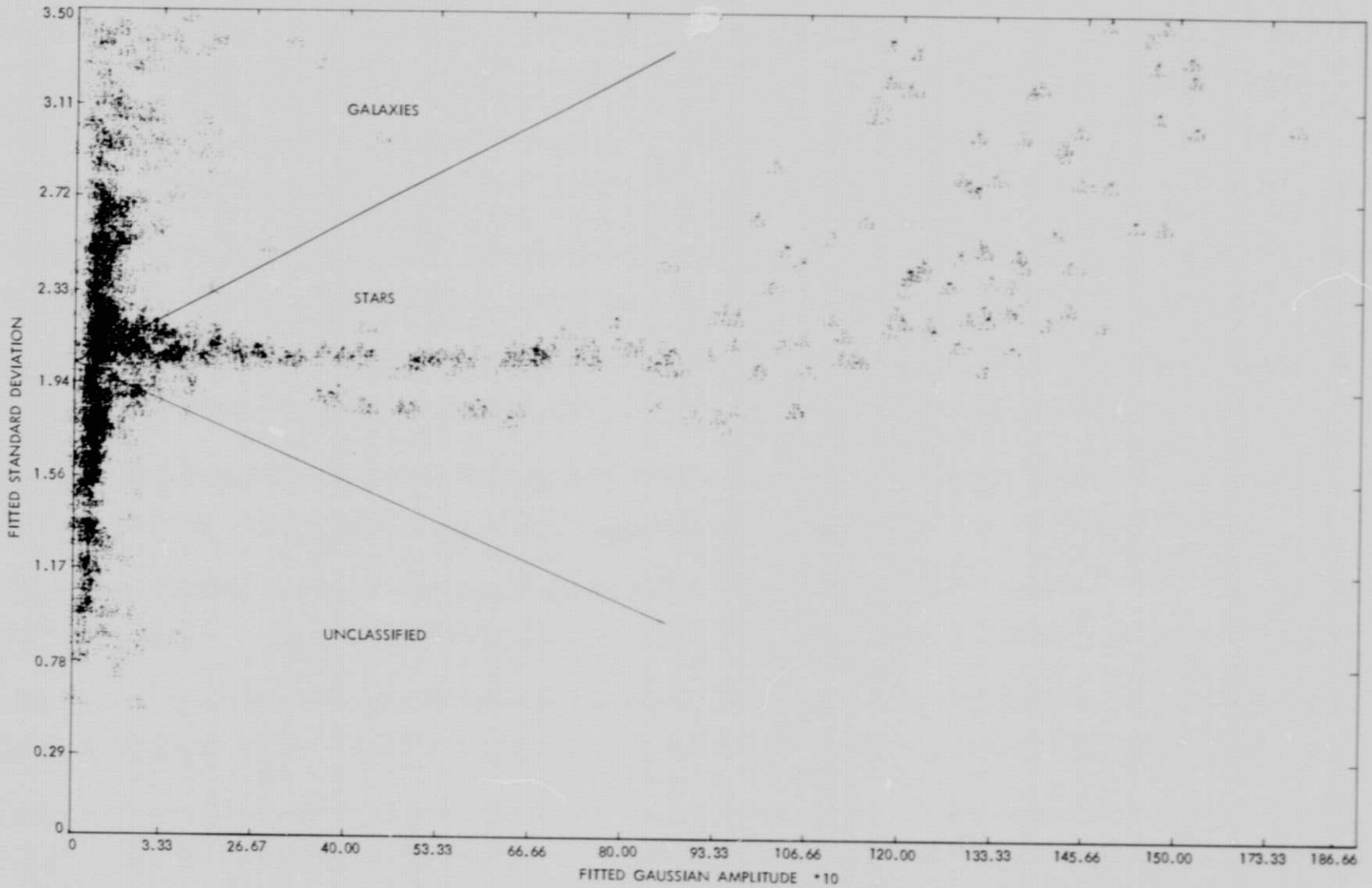

Figure 5. A plot of the classification space showing the distribution for the cluster of galaxies Abell 655. Both stars and galaxies are present, as indicated by the well-developed vertical and horizontal branches

(1) The vertical cluster above the horizontal cluster represents galaxies only.

(2) The horizontal cluster including the scatter of points to its upper right represents stars only.

(3) The vertical cluster below the horizontal cluster represents objects too faint to discriminate into classes.

Objects lying in the stellar region which, for some reason, had high eccentricities were classified as galaxies. This test was significant only at the intersection point between all three clusters and was the only contribution of the eccentricity parameter.

The diagrams can be understood intuitively. Galaxies compared with stars, will be disproportionately larger in width for the same amplitude and will thus fall into the upper left of the diagram. Stars would, if it were not for emulsion nonlinearity, possess identical standard deviations, irrespective of their amplitudes, and would lie along a horizontal line. The brightest stars become saturated, having disproportionately lower amplitudes, and thus would populate the upper right of the diagram. Very faint objects are distorted by the grain structure and tend to have small standard deviations. These objects fall into the lower left part of the diagram. It can be seen in the case of the two different exposure NGC6218 plots that as the exposure increases, stars travel up the vertical cluster, and then move to the right along the horizontal cluster. At this turning off point the galaxies continue to move upward, providing the segregations observed.

Figure 6 shows a picture of Abell 655, each object being identified with its ID number and a letter beneath signifying classification type. The letters are "S" for star, "G" for galaxy, and "U" for unclassified. Figures 7 and 8 show Abell 655 with only the galaxies and only the stars respectively as identified in Fig. 6. A distinct population gradient is apparent in Fig. 7. Several blended stars have managed to get into the galaxy classification, and some false "galaxies" have been triggered by the diffraction spikes of the brighter stars.

A great deal of useful information can be generated automatically by this type of algorithm. The classification allows the radial population density of galactic clusters to be readily analyzed. Radial profiles, produced for each object, allow tidal effects to be studied between cluster members.

The classifier processed about one object per second on an IBM 360/65 operating in a multitask environment. Typical objects were, in this case, about 20 pixels in diameter, and an image scan comprised 3000 by 3000 pixels.

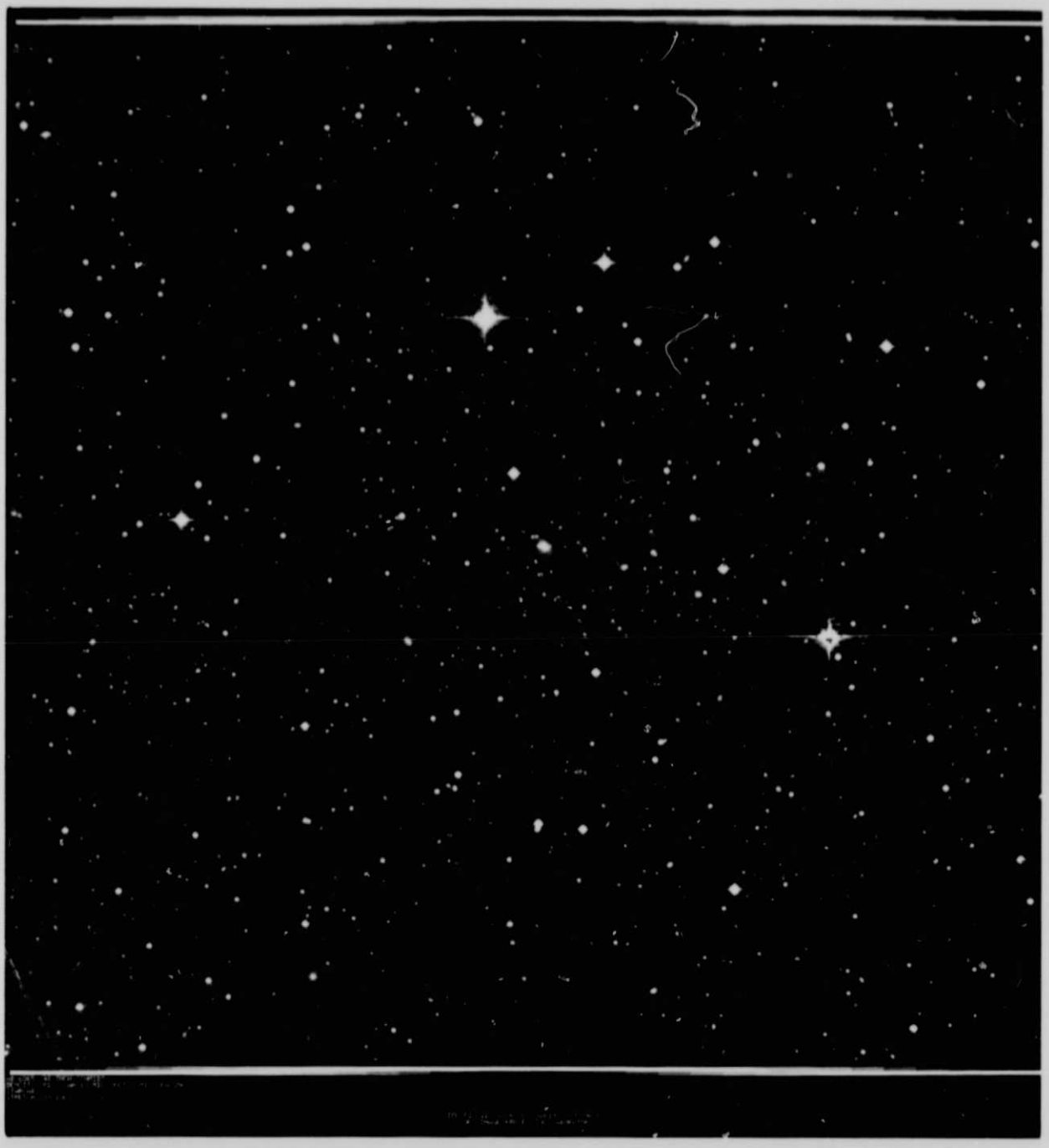

Figure 6. A classification chart of Abell 655 with each located object identified by number and class. The numbers are used to associate each object with a computed magnitude and radial intensity profile. The class is indicated as S for star, G for galaxy, and U for unclassified

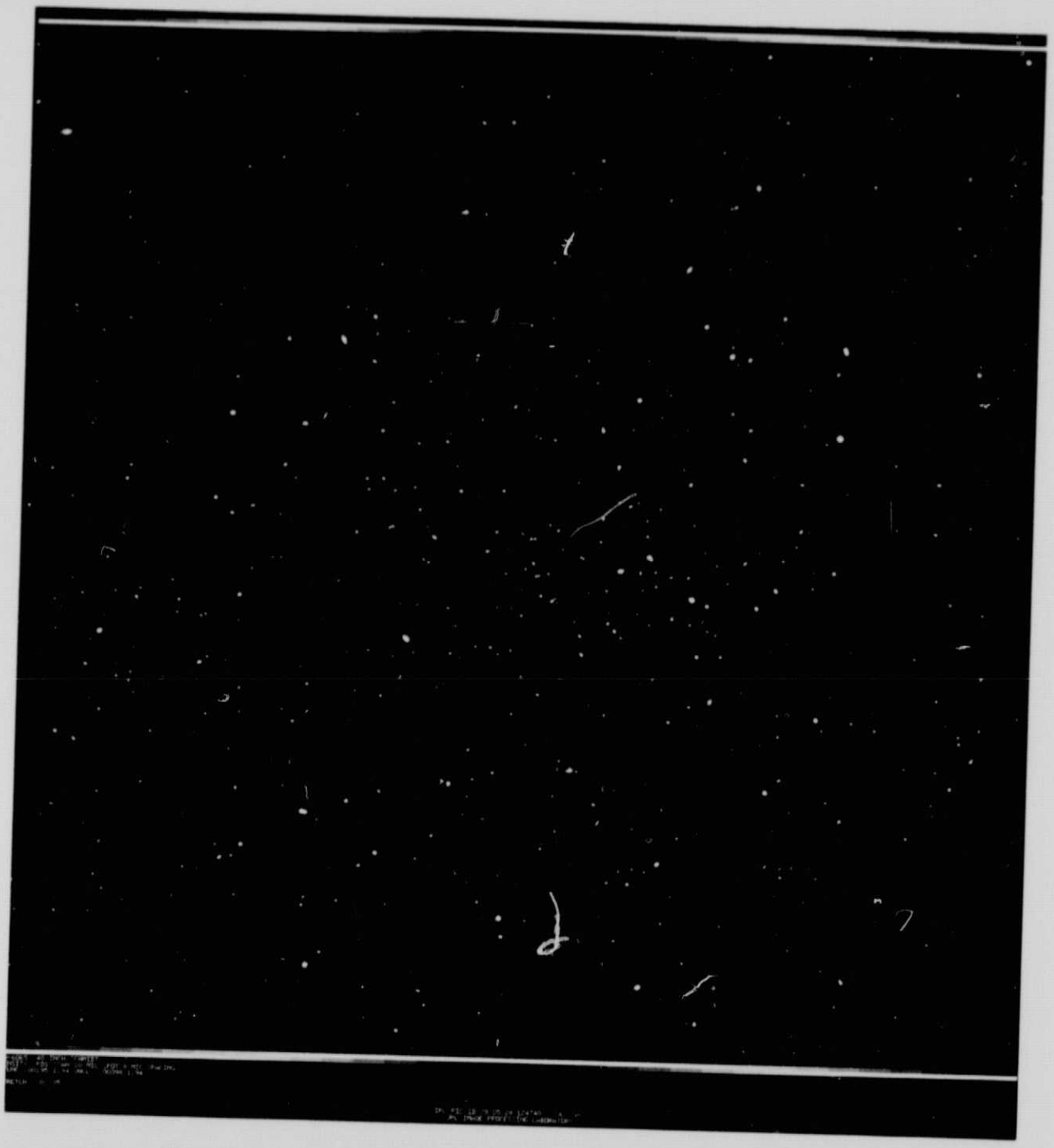

Figure 7. An image of only the galaxies in Abell 655. A few blended stars have been included

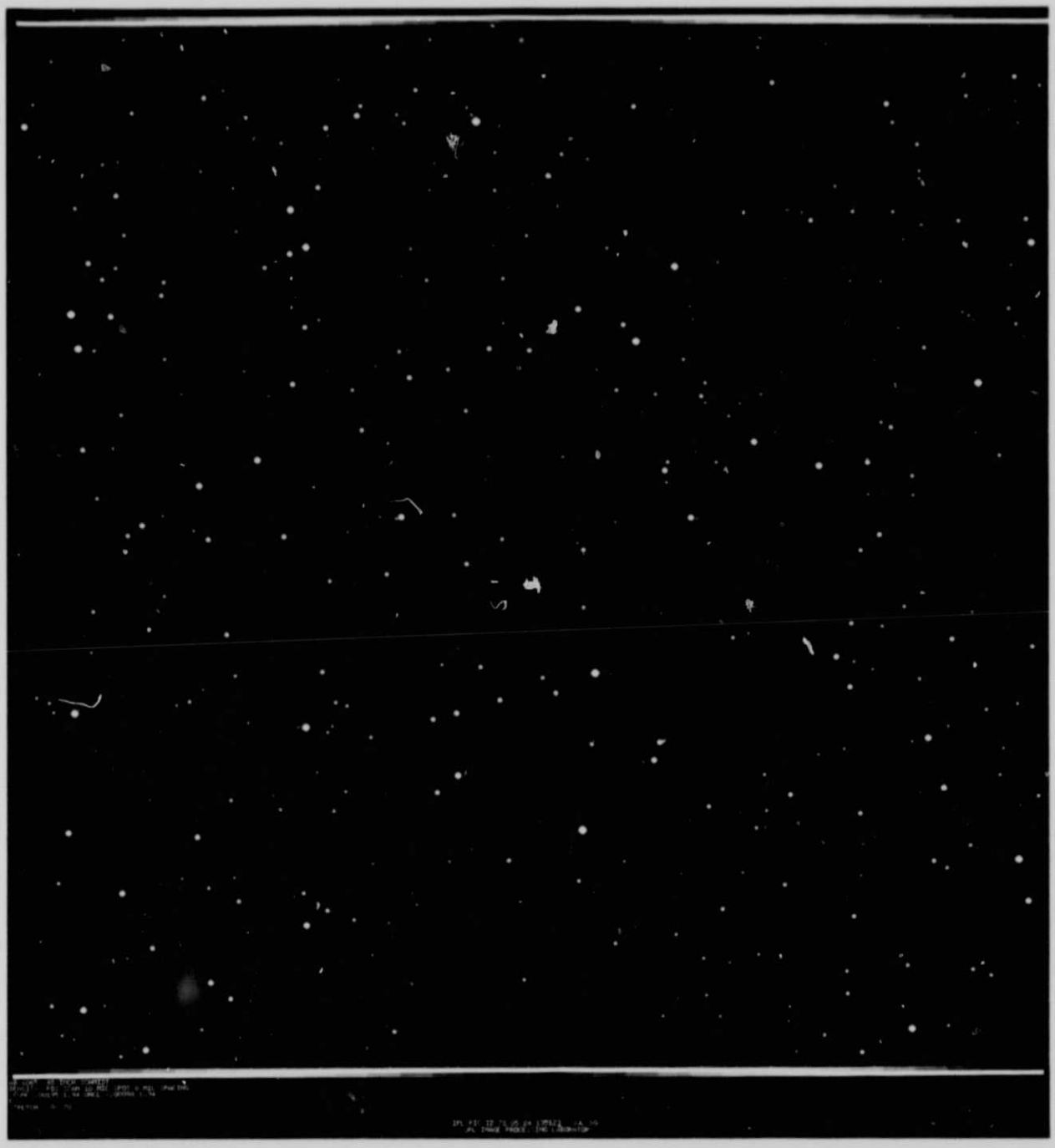

Figure 8. An image of only the stars in Abell 655

SECTION IV

DISPLAYS OF MULTISPECTRAL RADIO DATA

The purpose of this section is to illustrate three methods of displaying multispectral images of small size but containing numerous bands. This is essentially a three-dimensional problem which must be reduced to two dimensions by using some property of the human processor as an intermediary. The techniques consist of:

(1) Generating a mosaic of each image.

(2) Producing a color-coded image to depict radial velocity.

(3) Producing a stereo pair with radial velocity as depth.

A series of 50 radio images of the T Tauri object Lick Hα101 taken in the CO J=0,1 band were provided for analysis by Dr. Thomas Kuiper of JPL. The images were equally spaced in radial velocity. Each image subtends approximately 5 by 4 minutes of arc and contains 100 points.

In Figs. 9 and 10, a sequence of 20 images is presented covering a radial velocity range from +2.47 to -2.46 km/s. Beneath each image is the histogram of intensity values in that image. Each image has been scaled to a consistent system of intensity so that they can be compared. In this mode all of the information can be made visible but it is not all easily assimilated at one time.

A second approach combines all of the images into a single color-coded image. Three-color primary images were synthesized from the original pictures by combining them in weighted sequences. Thus, the blue image was the sum of all of the originals with negative radial velocity with progressively greater weight away from zero radial velocity. The red image was synthesized in the same manner as the blue one except in the opposite direction, and the green was weighted with a triangle function centered about zero radial velocity (Ref. 2). These three images were converted into hue, saturation, and intensity images (Ref. 1); the saturation image was contrast-enhanced to enhance colors and the inverse transformation was performed back to blue, green, and red images. These images were color-additively combined into the representations in Fig. 11. Both sides of Fig. 11 represent the same data, with the distinction that in the left picture, intensity is linear with reflectance, whereas in the right picture intensity is linear with density. This method of displaying the data allows a simultaneous evaluation of all bands at once. It is a good technique if the number of bands is small but less so if they are many due to the heavy demands made upon color discriminability. If the velocity distribution is chaotic rather than smooth, this limitation would be severe.

The third display method considers the data to consist of a cube where depth signifies radial velocity. A stereo pair was generated by creating two pictures which simulated views of the cube from symmetrically opposite sides, looking down from above. Each pixel in these views represented the integrated line-of-sight intensity of a view ray penetrating the cube

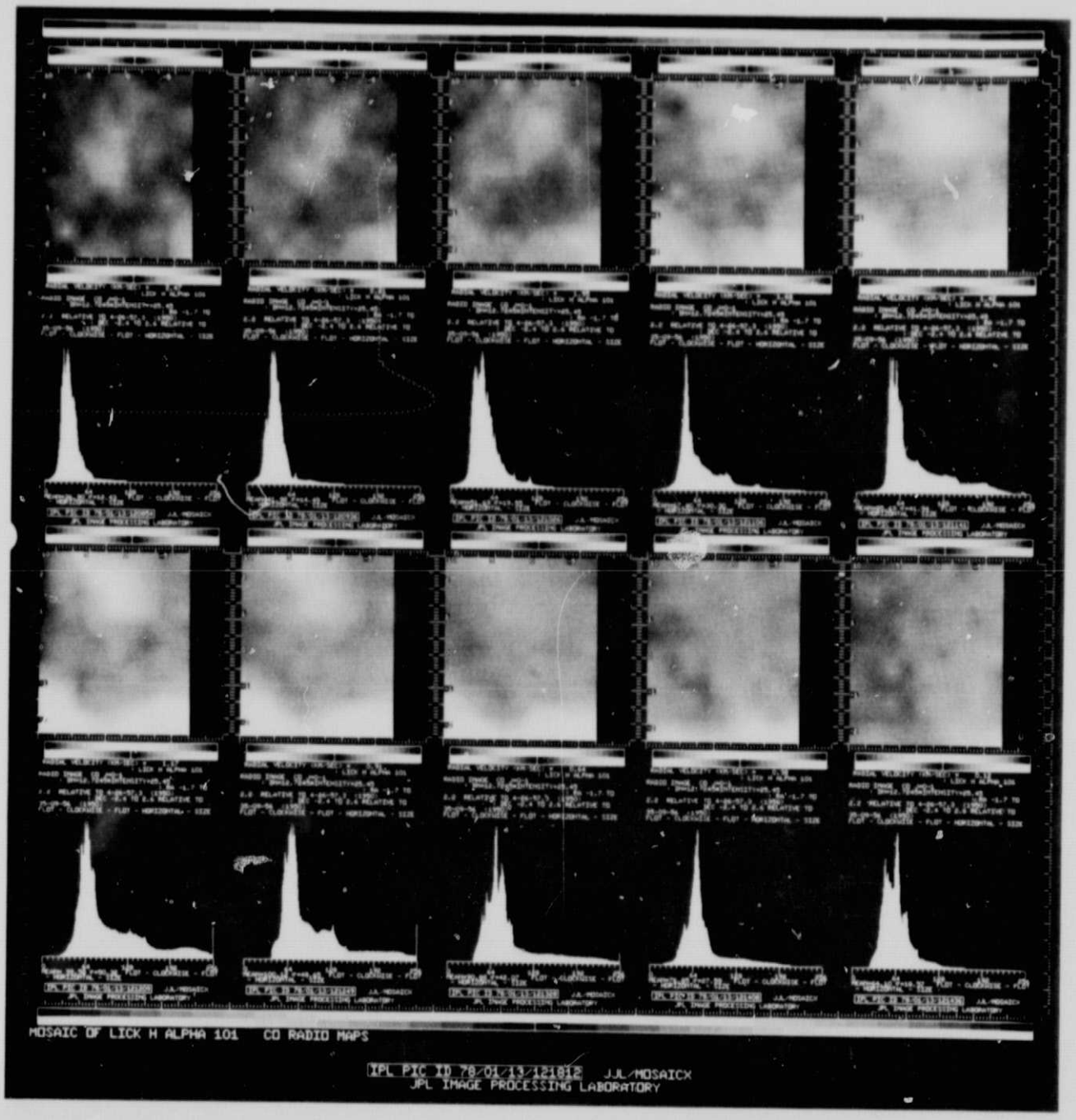

Figure 9. A mosaic of images of Lick Hα101 in the radio, each at a different radial velocity in the CO J=0,1 band. Positive radial velocities from 2.47 to 0.12 km/s

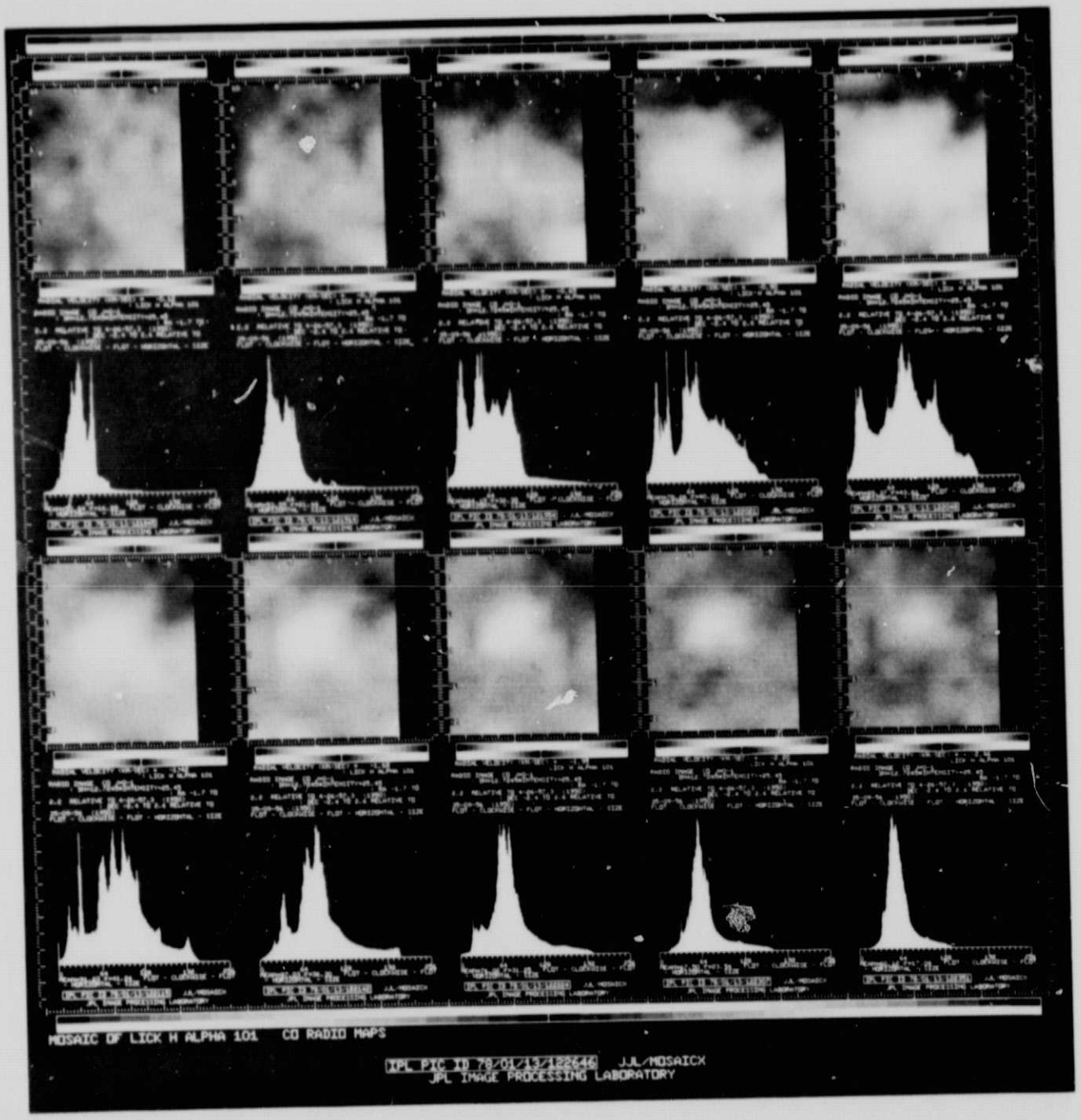

Figure 10. The same sequence of frames as in Fig. 9 continued from -0.12 to -2.46 km/s

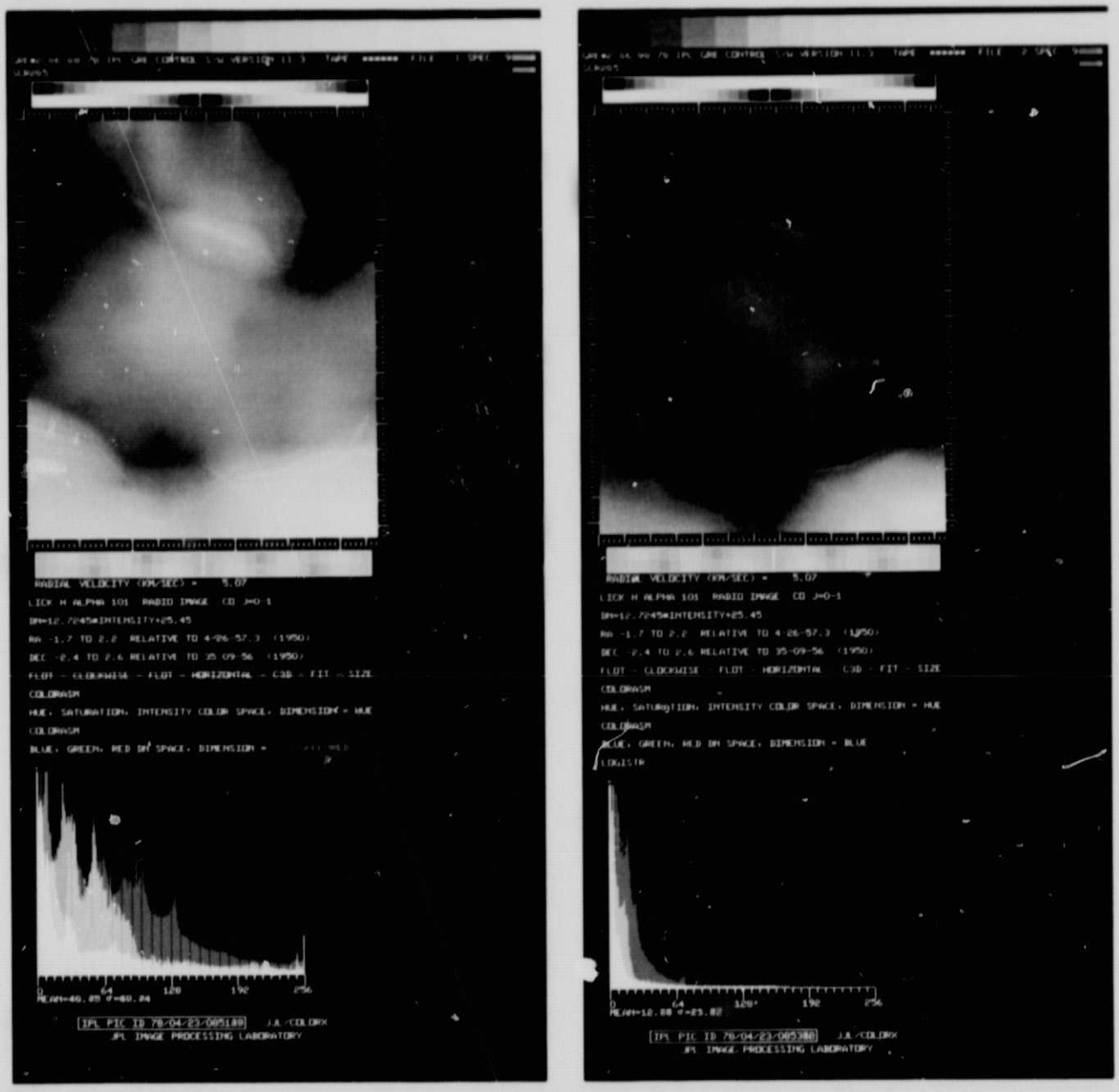

Figure 11. Two color images of Lick Hα101 each generated from three color images synthesized from the images of Figs. 9 and 10. The blue and red synthesized images were composed of sums of images weighted linearly by their distances from zero radial velocity. The green image was weighted by a triangle centered on zero radial velocity. In the left image, intensity is linear with reflectance. In the right image, intensity is linear with density

from one of two common eye positions above it. Two pairs of stereo views are presented in Fig. 12. The top pair is identical in geometry to the lower pair except for a 3-D grid of stereo cue dots present in the lower pair to aid in stereopsis registration.

One can see stereo with some difficulty by crossing one's eyes (the left eye sees the right image and the right eye sees the left image) and then registering the two images. The difficulty arises due to the very low spatial frequencies involved and the large viewing angle required between the two eyes in order to distinguish stereo in the case of low spatial frequencies. Negative radial velocity is down. The stereo method would operate well if the number of bands is high and if the spatial frequencies of the bands are also relatively high (the velocities chaotic), providing complex structure upon which to fuse and to generate the effect of stereo.

The last two methods complement each other because each operates optimally where the other is the least effective. In the above example case, the color display was most effective because of the low spatial frequencies, small picture size, and smooth nature of the velocity distribution.

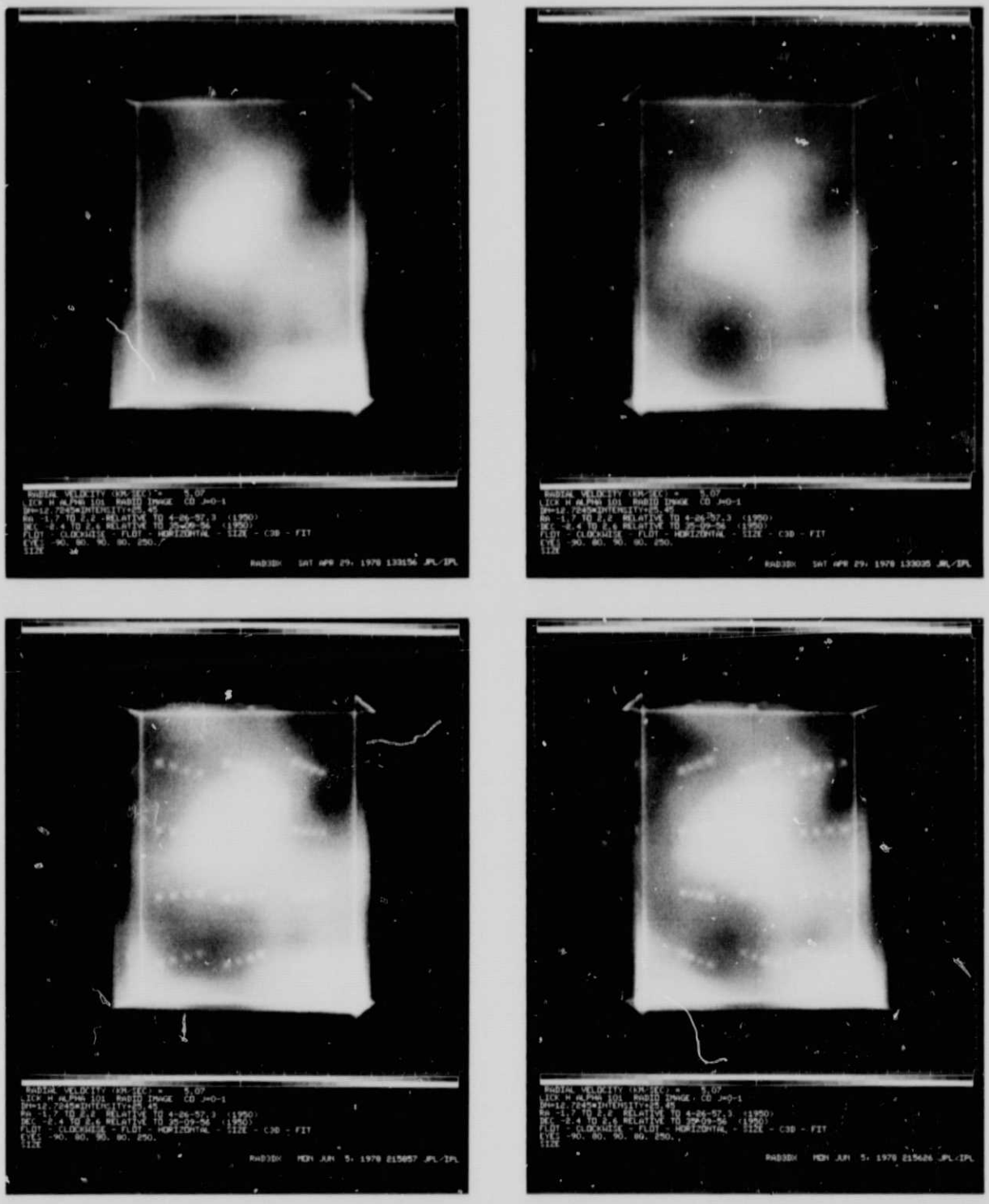

Figure 12. A mosaic of two stereo pairs of Lick Hα101 comprising the images of Figs. 9 and 10. The top two are one pair and the bottom two are another pair containing stereo cues. Stereo can be realized with some difficulty (owing to the low spatial frequencies of the data) by crossing one's eyes and focusing the two images

SECTION V

SUMMARY AND CONCLUSIONS

Image processing techniques were sucessfully applied to three areas of astronomy. Applications consisted of the decalibration of vidicon spectra, the segregation of stars from galaxies, and the display of multispectral radio images. From inspection of the resulting application of these processes, the following conclusions can be reached:

(1) Vidicon spectra can be accurately corrected for geometric distortion without a degradation in resolution. This process can routinely be performed on a custom basis by a program and does not require human intervention.

(2) Vidicon spectra can automatically be radiometrically corrected to remove positionally dependent sensitivity. An acceptable relative correction can be performed even if an absolute calibration standard is not available.

(3) Intensity plots of digital vidicon spectra can be obtained automatically by decalibrating the images and removing the night sky background by interpolation. This allows the generation of high-quality spectra with the large dynamic range and good signal-to-noise provided by the vidicon.

(4) Digital pictures of clusters of galaxies can be processed by programs which distinguish between stars and galaxies. The classification parameters are the radial standard deviation, the gaussian amplitude, and the photometric eccentricity. Aside from human intervention required to partition the classification space, the process is performed automatically.

(5) Each object in a picture can be analyzed to produce its eccentricity, intensity, axial orientation, radial intensity profile, and azimuthal intensity distribution. This process is automatic and can be performed inexpensively on a large number of objects. From this information, tidal shear effects of galactic halos can be studied.

(6) Once a classification has been performed, pictures can be generated containing only the stars or only the galaxies. These displays facilitate analysis of the distribution of galaxies in clusters.

(7) Multispectral radio maps comprising numerous bands can be displayed in at least three forms. Mosaics of individual frames with associated histograms provide a complete record, but are difficult to analyze simultaneously. Color-coded radial velocity is useful when the number of spectral bands is small and the radial velocities are not too complex. Stereo pairs visualizing depth as radial velocity are useful if the eye can register the images. Registration and stereopsis

require a large number of bands and considerable high spatial frequency structure.

It is hoped that some of the above ideas will inspire others to apply image processing techniques to astronomical imagery. This is a rapidly expanding field whose potential remains as yet untapped. The author invites communication and the exchange of information.

The specific techniques developed in this report depend upon software written expressly for this purpose. However, great reliance was placed upon general purpose programs developed for the support of other projects and it was due to this environment that timely use could be made of human resources. In particular, capabilities developed for the Viking and Voyager Projects were applied in this study.